Efficiency of Cathodoluminescence Emission by Nitrogen-Vacancy Color Centers in Nanodiamonds

*Huiliang Zhang, David R. Glenn, Richard Schalek, Jeff W. Lichtman, and Ronald L. Walsworth**

Correlated electron microscopy and cathodoluminescence (CL) imaging using functionalized nanoparticles is a promising nanoscale probe of biological structure and function. Nanodiamonds (NDs) that contain CL-emitting color centers are particularly well suited for such applications. The intensity of CL emission from NDs is determined by a combination of factors, including particle size, density of color centers, efficiency of energy deposition by electrons passing through the particle, and conversion efficiency from deposited energy to CL emission. This paper reports experiments and numerical simulations that investigate the relative importance of each of these factors in determining CL emission intensity from NDs containing nitrogen-vacancy (NV) color centers. In particular, it is found that CL can be detected from NV-doped NDs with dimensions as small as ≈40 nm, although CL emission decreases significantly for smaller NDs.

1. Introduction

The realization of structural imaging with suboptical resolution in conjunction with nanoscale localization of molecular labels in the same field of view is an important challenge in electron microscopy (EM), with great potential impact in both the life and physical sciences.[1,2] In recent years, various approaches toward this goal have been pursued, including marking distinct epitopes with (i) different sizes[3] or shapes[4] of nanoparticles (NPs) that provide electron density contrast; (ii) NPs with distinguishable energy-dispersive X-ray contrast;[5] and (iii) NPs with visible wavelength (color)–distinguishable cathodoluminescence (CL) contrast.[6] Among these methods, NP CL is the newest and perhaps the most promising, given its high detection sensitivity[6,7] and the unambiguous spectral separability of such labels.

Cathodoluminescence is the light emitted during relaxation of electronic excitations in a solid, generated by interaction with an electron beam.[2,8,9] CL emission at visible wavelengths (photon energies ≈1 eV, typically generated using electron beam energies of 100 eV to 300 keV) has been used extensively as a probe of material properties, with a variety of recent applications that include probing plasmonic modes in metallic nanostructures,[10,11] observing nanoparticles on a polymer film,[12] and measuring light emission by nanoscale semiconductor heterostructures.[13] The wavelength of CL emission is determined by the electronic energy levels excited[14] and can be controlled to some extent in semiconductors and insulators (such as diamond) by doping or implanting color centers or other defects with well-known

Dr. H. Zhang, Dr. D. R. Glenn, Prof. R. L. Walsworth
Department of Physics
Harvard University
Cambridge, MA 02138, USA
E-mail: rwalsworth@cfa.harvard.edu
Dr. R. Schalek, Prof. J. W. Lichtman
Department of Molecular and Cellular Biology
Harvard University
Cambridge, MA 02138, USA
Dr. R. Schalek, Prof. J. W. Lichtman, Prof. R. L. Walsworth
Center for Brain Science
Harvard University
Cambridge, MA 02138, USA
Prof. R. L. Walsworth
Harvard-Smithsonian Center for Astrophysics
Cambridge, MA 02138, USA

DOI: 10.1002/smll.201700543

 © 2017 Wiley-VCH Verlag GmbH & Co. KGaA, Weinheim

emission spectra into the host crystal. It has been shown[6,15] that multicolor nanoscale molecular localization in EM can be achieved by employing several independent types of defect-containing NPs as markers, with each NP type producing spectrally distinct CL and capable of being conjugated to ligands with high affinity for a specific molecular target.

The nitrogen-vacancy (NV) color center[16,17] in diamond[18,19] is of particular interest for applications in correlative CL and EM imaging, emitting primarily in the red ($\lambda \approx 575$–750 nm) region of the spectrum. The NV center has been widely investigated because of its unique optical and spin properties, and NV centers in nanodiamonds (NDs) have been employed in diverse optical imaging applications, such as super-resolution imaging by stimulated-emission depletion,[20] long-term in vivo tracking of transplanted stem cells,[21] and local intracellular temperature monitoring.[22] The well-described optical properties of the NV center in NDs make it an ideal system for detailed study of the CL emission in NPs.

For molecular localization applications in EM, markers should be both small, for high spatial resolution and efficient staining in tissue, and bright, for rapid and reliable imaging. In the present work, we investigate the dependence of NV-ND CL emission intensity on a variety of parameters, including e-beam energy and intensity, ND size, and NV density. We present an empirical model describing how these parameters influence CL intensity, and perform a series of correlated scanning electron microscope (SEM), photoluminescence (PL), and atomic force microscope (AFM) measurements to characterize each parameter, with the goal of estimating the minimum size of particles that can be used to generate detectable CL signals. In particular, we study the scaling of CL intensity with ND size, and conclude that surface effects (i.e., either increased rates of carrier recombination at the surface, or quenching of NV fluorescence due to interaction with localized surface states) are not an important factor limiting CL intensity emitted from NDs of size $d > 50$ nm. We observe detectable signals from particles as small as $d \approx 40$ nm, limited primarily by the signal-to-noise ratio of our CL imaging setup.

2. Parameters Determining CL Intensity

We first introduce a phenomenological expression for the dependence of emitted CL intensity on electron beam parameters and the size of the probed ND. Electrons impinging on the diamond have an energy-dependent cross section for inelastic interactions with the crystal, resulting in a finite energy deposition efficiency (defined as the ratio of total energy deposited to initial kinetic energy of a single incident electron), denoted $\eta(V, d)$. This quantity depends in general on the accelerating voltage V, and the particle size d that determines interaction length of the electron passing through the nanocrystal.

Of the energy deposited in the crystal by inelastic scattering of the incident electrons, only a fraction produces electronic excitations in the native NV centers, which then decay radiatively and give rise to detectable CL. This conversion efficiency, here denoted ξ, will in general be an average over individual energy conversion efficiencies for each NV center in the particle, which may vary due to details of the local crystal environment such as the density of nearby electron donors (typically substitutional nitrogen defects), surface states, etc. However, the carrier diffusion length[23] in the NDs of interest is comparable to or larger than the particle size (typically 20–200 nm in diameter), precluding spatially resolved electron beam excitation of individual NV centers. We can therefore measure only the integrated CL from the full particle, and must consider the average conversion efficiency $\bar{\xi}$, such that $\xi = N \times \bar{\xi}$, with N the number of NV centers present in the particle. Due to possible saturation effects arising from the finite radiative lifetime of the NV centers, this efficiency can depend on the electron beam current I. Furthermore, we conjecture that $\bar{\xi}$ may also depend on the particle size, since smaller particles may have higher rates of carrier recombination at surfaces, resulting in a reduction of the average energy conversion efficiency to CL photons. We parameterize the particle size for this purpose with the linear dimension $d = v_{\mathrm{ND}}{}^{1/3}$, where v_{ND} is the ND volume measured by SEM and AFM. Taking all of these factors into account, we expect that the total observed CL signal intensity S_{CL}, integrated over the area (A) and angular acceptance (Ω) of the detection optics, is given by:

$$S_{\mathrm{CL}}(V,I,d) = \int s_{\mathrm{CL}}\, dA\, d\Omega \propto (V \times I) \times \eta(V,d) \times N \times \bar{\xi}(I,d) \tag{1}$$

Here, the integrated CL intensity has units of power, as does the energy flux of the electron beam ($V \times I$), while the NV number, energy deposition and energy conversion factors are dimensionless. In practice, the electron beam diameter (limited in our experiments to ≈4 nm by diffraction in the best case, and more typically to ≈20 nm due to defocus and/or sample charging) is much smaller than the NDs, such that the CL image of each particle is distributed over many detection pixels. (Pixel size is determined by electron beam raster parameters, and is chosen to match the electron beam diameter.) In the experiments that follow, we consider only the peak CL intensity, which generally occurs as the beam passes over the center of each ND. Using correlated CL, SEM, PL, and AFM imaging, we calibrate the dependence of S_{CL} on V, N, and η, and thereby measure $\bar{\xi}$ as a function of d.

3. Characterization of Nanodiamond Shape and Size

We began by measuring the size distribution and morphology of the NDs under investigation. For the purpose of this study, we looked at He^+-irradiated, type Ib NDs, which contain the highest NV concentration of any commercially available sample currently known to us (see the Experimental Section for details). Preliminary analysis by dynamic light scattering in aqueous suspension indicated a mean hydrodynamic diameter of 82 nm, with standard deviation 22 nm. We then prepared a sample of NV-containing NDs on a silicon

 © 2017 Wiley-VCH Verlag GmbH & Co. KGaA, Weinheim

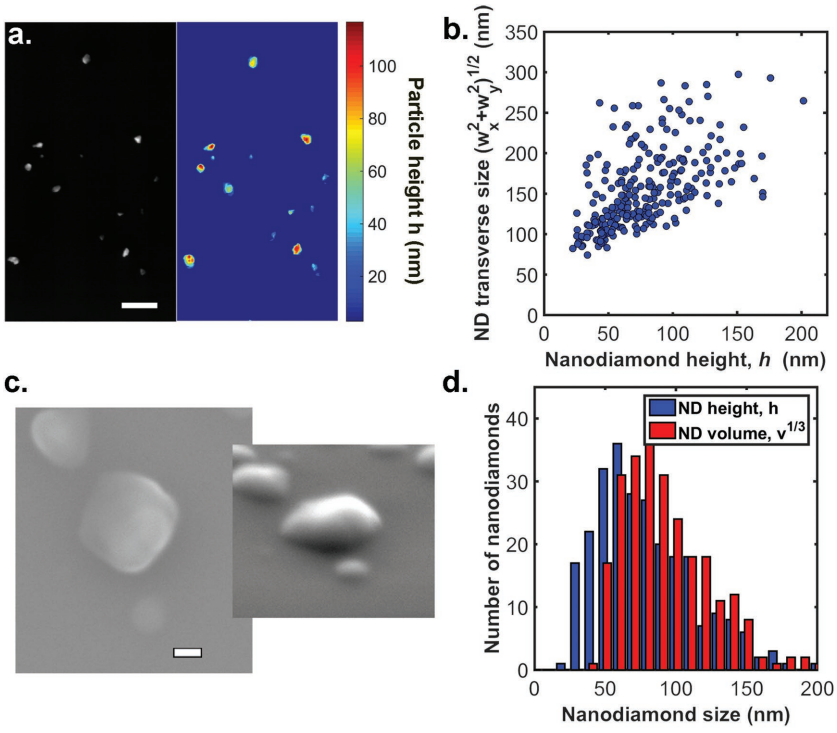


Figure 1. Characterization of nanodiamond (ND) size and morphology. a) NDs, dispersed on Si wafers, were imaged using correlated secondary electron imaging (SE, left panel) and atomic force microscopy (AFM, right panel) to determine their transverse (w_x, w_y) and longitudinal (h) dimensions, respectively. SE provides a better estimate of transverse dimensions than AFM due to blurring associated with finite tip radius. SE scale bar is 1 µm. b) ND aspect ratios for all particles ($n = 257$) in our sample. Most particles were found to be plate-like, with aspect ratios w/h between 1.5 and 3. c) Zoomed-in SE images of several NDs from our sample on a tilted stage, illustrating the plate-like morphology of the particles. Left panel shows dimensions of NDs in the plane parallel to the silicon wafer (i.e., w_x and w_y); right panel shows the same field of view tilted 60° toward the normal. Scale bar is 100 nm. d) Histogram of particle sizes, d, calculated using both the shortest dimension h and the geometric average $v^{1/3} = (w_x \cdot w_y \cdot h)^{1/3}$. We use the latter definition in all subsequent measurements.

wafer and imaged 20 fields of view in both AFM and SEM (**Figure 1**a). (Also see Figure S1 of the Supporting Information for a complete set of correlated microscopy data for one field of view.) Measurements were made for a total sample size $n = 257$ particles. The transverse dimensions, w_x and w_y of each particle were obtained from the secondary electron SEM images, while particle heights h were extracted from the AFM measurements. The NDs tended to be ellipsoidal or plate-like, with the shortest dimension h perpendicular to the substrate surface (Figure 1b,c). Unless otherwise indicated, we used the average dimension $d = (w_x \times w_y \times h)^{1/3}$ to parameterize ND size for all further measurements, because (i) this was the most appropriate value to describe achievable CL labeling resolution, and (ii) it was most relevant for estimating the number of NV centers per particle, assuming constant NV density. We note, however, that we repeated most analyses with the alternative parameterization $d_{alt} = h$, since this generally sets the shortest distance between any point on the interior of a given ND and the nearest surface, which may be most relevant for surface-related quenching and recombination effects in small particles. In our measurements and analyses, no significant difference was observed between the two parameterizations. The distribution of d values for our ND sample was peaked at 93 nm, with a standard deviation of 32 nm (Figure 1d).

4. Calculated Energy Deposition Efficiency $\eta(V, d)$ and Comparison to Measured Signal S_{CL}/V

We studied the dependence of the deposited energy fraction for incident electrons η, on the e-beam accelerating voltage V, and the size, d, of the NDs probed. Because the rate of inelastic energy loss decreases with electron energy ($dE/dz \sim E^{-2/3}$ in the model of Kanaya and Okayama,[24]) we expected that highly energetic incident electrons should pass ballistically through the NDs with minimal energy loss, whereas extremely low energy electrons should be completely stopped. Thus, for efficient generation of CL emission in particles of a given size, some intermediate electron energy corresponding to a stopping range close to the particle size should be optimal. This prediction was supported by preliminary numerical calculations made using the CASINO software package[25,26] (Figure S2, Supporting Information).

To observe $\eta(V, d)$ experimentally, we repeatedly imaged a subset of NDs in CL, while varying the electron accelerating voltage V (**Figure 2**a). The goal of this procedure was to provide empirical support for our numerical model of η, to justify its use for normalizing CL intensities (and thereby isolating ξ) in later experiments. The comparison between experiment and model was carried out under the assumption that the efficiency of conversion from deposited energy to CL intensity ξ remained constant during the measurement for any given particle, as V was varied. The V-dependence of the deposition efficiency η for that particle could thus be determined from the observed CL intensity since, from Equation (1), $\eta(V, d) \propto S_{CL}/V$ when I, N, and ξ are held constant.

All CL images were obtained with an e-beam current of 1 nA, well above the observed saturation current (defined as the current at which observed CL rate reaches half of its large-current asymptotic value) for NDs in the size range of interest (Figure S3, Supporting Information). Because we could measure only S_{CL} vs V, while ξ was unknown for any particular particle, the deposition efficiency η was determined only to within a constant for each ND. (The conversion efficiency ξ might vary considerably between NDs, depending on the relative number of NVs and other carrier recombination sites, and possibly also the ND size. We had no a priori model for the dependence of ξ on other ND parameters.) To enable

 © 2017 Wiley-VCH Verlag GmbH & Co. KGaA, Weinheim

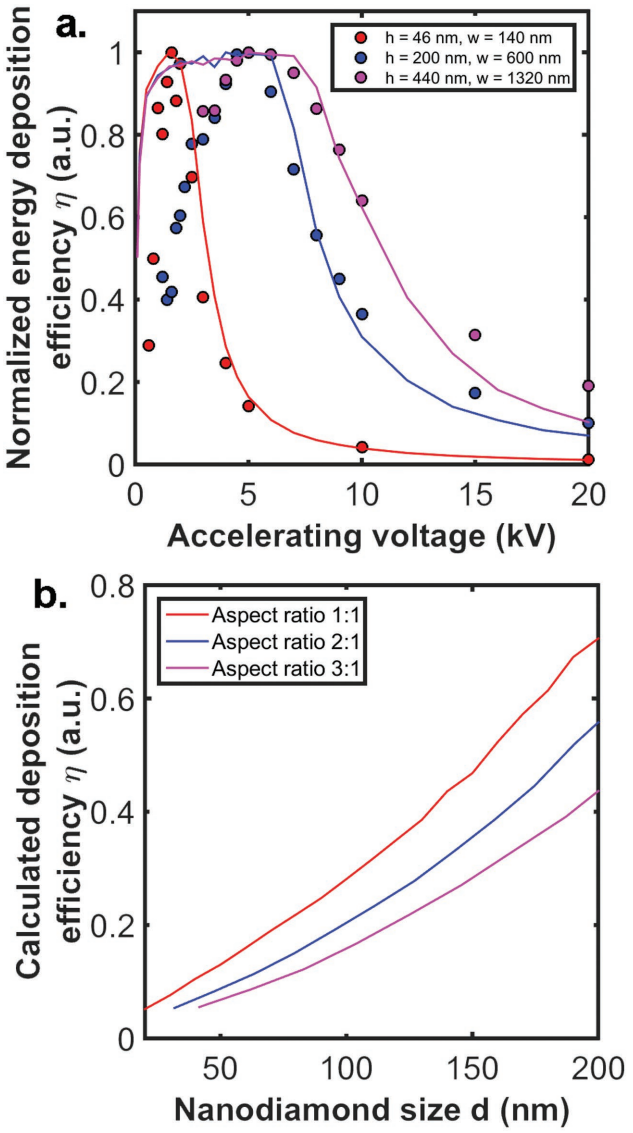


Figure 2. Calculated energy deposition efficiency, η, and comparison with measurements. a) Filled dots: Measurements of the voltage-corrected cathodoluminescence (CL) signal, S_{CL}/V, which is expected to be proportional to the electron energy deposition efficiency η. (Each set of points is independently normalized to 1.) Data are shown for three particles with widely varying size parameters to rigorously test our model for η. Solid lines: CASINO calculations of energy deposition efficiency η (also normalized to 1), for model particles of the same dimensions. The CASINO model particles are prolate ellipsoids, with diameter w in the two transverse directions, and height h in the axial direction. The calculated values agree well with observation for the parameter range of interest (V = 5 kV, d = 20–200 nm, similar to the data shown in red), but deviate for larger particles (blue, violet) at low V, likely due to surface carrier recombination. b) Typical CASINO calculations of absolute deposition efficiency η (now without normalization) for a range of particle sizes d and aspect ratios h/w, where $w = w_x = w_y$ are the ND transverse dimensions, and h is the ND height along the direction of e-beam propagation. The simulated accelerating voltage is V = 5 kV. The variation in η for different aspect ratios illustrates the importance of using an ellipsoidal model to describe NDs, rather than a simple sphere.

comparison with the CASINO calculation (which contains no information about ξ), we normalized both the measured S_{CL}/V and the calculated η to a peak value of 1 for each ND. As expected, the voltage-corrected CL signal S_{CL}/V took on a maximum value at an accelerating voltage on the order of a few keV, which was repeatable for particles of a given size d, and increased with increasing d. CASINO simulations of energy deposition efficiency were carried out using model NDs with prolate ellipsoidal geometry, $w_x = w_y \equiv w \geq h$, for w the diameter in the transverse dimensions and h the axial height. The simulations showed similar behavior of S_{CL}/V as a function of voltage, although the measured S_{CL}/V dropped off faster at low V than predicted by the model. This discrepancy was likely due to increased surface recombination of carriers generated by low-energy electrons that were stopped immediately upon entering the crystal; thus, at low V, the assumption that ξ is independent of V may not be strictly correct. Nevertheless, for ND sizes in the range of 20–200 nm (typical of our main ND sample) and $V > 2$ keV, the model matches the data well enough to justify its use for estimating $\eta(V, d)$. We also calculated the deposition efficiency $\eta(V = 5$ keV, $d)$ as a function of particle size d and aspect ratio h/w, where the model particles were again taken to be prolate ellipsoids, and $d = (w_x \times w_y \times h)^{1/3}$ (Figure 2b). It was clear from this calculation that, for NDs in the size range of interest, η can vary significantly as a function of the ND aspect ratio. We therefore used the prolate ellipsoidal model (rather than simple spherical NDs with diameter d) in CASINO calculations to correct for the effect of η in all subsequent CL measurements.

5. Number of NVs per Particle *N*

To estimate the number of NV centers present in each ND, we made quantitative PL measurements with a home-built confocal microscope.[27] We first calibrated the system using a separate sample of NDs (mean size ≈30 nm) with low NV density (nominally 1–3 NVs/ND), to determine the expected mean photon count rate for a single NV center. We scanned a circularly polarized excitation beam at 532 nm with intensity slightly above saturation (≈100 kW cm^{-2}) over the sample, split the detected fluorescence into two equal channels, and measured correlations in photon arrival times to isolate NDs containing only a single NV (**Figure 3**a). Interference filters in the detection path were chosen to admit PL emission from NVs in the neutral (NV^0) and negative (NV$^-$) charge states, since both produce CL under electron beam excitation.[28] For NDs containing a single emitter, we could distinguish NV charge states by the presence or absence of a bunching shoulder in the $g^{(2)}$ data associated with shelving in the NV$^-$ electronic dark state.[29] However, no correlation was found between the charge state determined by this method and the measured PL count rate, so all NDs containing single emitters were counted together as part of a single distribution (Figure 3b). Over the full sample NDs probed that contained single NV centers (n = 23), the mean photon count rate was ≈37 kilocounts per second (kcps), and the standard deviation was 10 kcps. We attribute the large width of this distribution to a combination of possible systematic factors including: (i) variability in the projection of the laser polarization onto the NV electric

 © 2017 Wiley-VCH Verlag GmbH & Co. KGaA, Weinheim

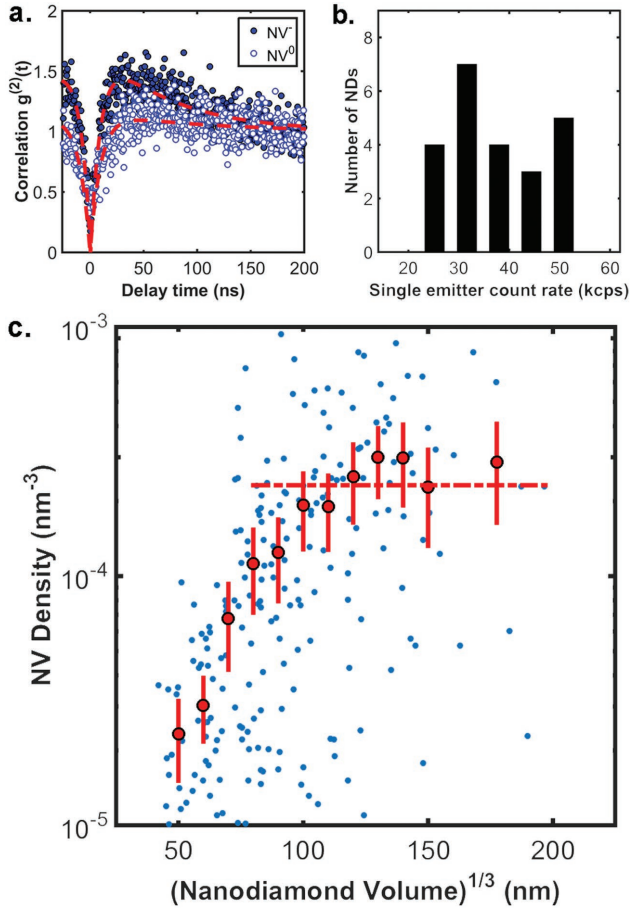


Figure 3. Photoluminescence (PL) counting of NV centers. a) Characteristic second-order autocorrelation time trace $g^{(2)}(t)$ used to identify NDs containing a single photon emitter (solid blue dots NV^-, open blue dots NV^0, and red dashed lines fits to experimental data).[22] NDs containing >1 emitter would show nonzero fluorescence at zero delay. b) PL intensity calibration of our confocal microscope carried out using only NDs containing single NV centers. The excitation beam was circularly polarized, with wavelength 532 nm, and intensity ≈100 kW cm^{-2}. The distribution of observed count rates per NV was assembled from n = 23 observations of single-emitter NDs, and has mean $\langle S_{PL}\rangle_{cal}$ = 37 kcps and standard deviation $\sigma_{PL,cal}$ = 10 kcps. The number of NVs in a brighter ND can be estimated as $N_{NV} = S_{PL}/\langle S_{PL}\rangle_{cal}$, with instrumental uncertainty $\sigma_{N,inst}$ = 10/37 N_{NV}. c) Density of NV centers for each ND in our main sample (n = 257), obtained by dividing measured NV number (using calibrated PL) by ND volume (from AFM and SEI images). Blue points show raw data for each ND, red circles are binned averages. Error bars are the quadrature sum of the instrumental uncertainty and the statistical standard error in the mean of each bin, $\sigma_{N,Tot} = (\sigma^2_{N,inst} + \sigma^2_{stat}/n_j)^{1/2}$, where n_j is the number of data points averaged in the jth bin. Data are consistent with a constant average NV density of (2.3 ± 0.2 S.D) × 10^{-4} nm^{-3} for NDs in the size range $d \geq$ 100 nm, indicated by the dashed red line. This density falls off rapidly for smaller NDs, possibly due to decreased efficiency of NV formation.

dipole axes due to random orientation of the nanocrystals (mitigated only in part by the use of circular polarization); (ii) possible photo-induced charge dynamics that primarily affect NVs within ≈10 nm of the ND surface and result in intermittent PL blinking,[30] potentially involving transitions to states out of the $NV^- - NV^0$ system;[31] and (iii) variability in the NV excited state lifetime due to proximity and orientation of the NV dipole relative to the interface between the ND and the silicon wafer substrate.[32] In the absence of a comprehensive model for the weights of these contributions (each of which may or may not be correlated between multiple NVs in the larger NDs of our main sample) to the observed count rates, we conservatively use the full width of the calibration PL distribution as our instrumental uncertainty for all subsequent NV number measurements.

We collected correlated PL images of our primary ND sample (n = 257, previously imaged in SEM and AFM), using the same optical excitation intensity and detection filters as for the single-NV PL calibration. This allowed us to estimate the NV number density for each particle (Figure 3c), which averaged about 2×10^{-4} nm^{-3} for NDs larger than $d \approx 100$ nm, but was significantly lower for smaller NDs. The observed dependence of NV density on d is not consistent with an excluded volume model, in which the effective dimensions of NDs are reduced to account for surface quenching or overestimation of w_x and w_y due to SE image defocus (Figure S4, Supporting Information). We therefore conclude that NV formation was suppressed during sample preparation for small NDs, likely because of some combination of reduced efficiency of vacancy generation by energetic He^+ ions and rapid migration of vacancies to nearby surfaces during annealing. For the 40 keV He^+ implantation protocol used to generate vacancies, our numerical simulation using the SRIM software package[33] predicts that the most efficient depth for vacancy generation in bulk diamond is ≈150 nm, larger than the size of most of the NDs.

6. Measured CL Intensity Distribution and Energy Conversion Efficiency $\bar{\xi}(I,d)$

We obtained CL images of the same NDs, colocalized with the AFM and PL fields of view described above, to study the efficiency of conversion from deposited e-beam energy to detectable CL. The CL data were collected with an e-beam current I = 1 nA, at constant accelerating voltage V = 5 kV. Analysis of the CL images reveals that, for NDs with nonzero PL signals, the fraction that produce observable CL decreased with particle size for d < 100 nm (**Figure 4**a, inset). The smallest NDs detectable by CL in our system were in the range of 30–40 nm, although only about 10% of the particles in this size range could be distinguished from the noise floor at the 5σ level.

To inform future applications in correlative CL imaging, we wished to determine whether this limited detection rate for small NDs known to contain one or more NV emitters was due to (i) the low CL brightness per NV making it difficult to distinguish from background the signal from NDs containing only a few NVs, or (ii) some additional size-dependent effect such as CL quenching or surface carrier recombination in small NDs suppressing CL emission per NV below the level observed in larger NDs. Therefore, by direct comparison with PL images, we measured the CL signal intensity as a function of the number of NV emitters in each ND (Figure 4a). We found that the dependence was linear down to the noise floor of the CL images, which became dominant

 © 2017 Wiley-VCH Verlag GmbH & Co. KGaA, Weinheim

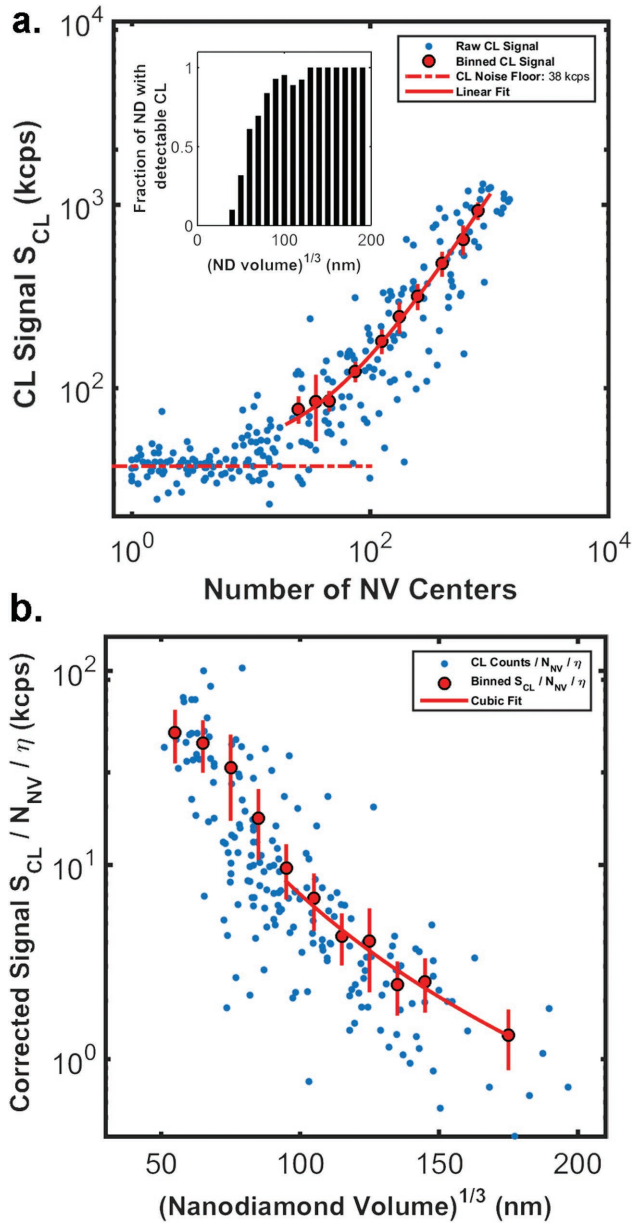


Figure 4. Effect of ND size and NV number on CL intensity. a) Measured CL signal as a function of number of NV centers (determined by PL intensity) for each ND sampled. Blue points show CL signal for all NDs; red circles are averages binned by NV number. The observed dependence is linear. (Solid red line shows a fit of the form $S_{CL} = c_1 N_{NV} + c_2$, with slope c_1 = (1.09 ± 0.03 S.D.) kcps/NV center.) The smallest number of NV centers detectable is on the order of 10–20, before background noise (red dotted line) becomes dominant. This suggests that NV density will also determine the size limit for CL detection. Inset shows fraction of NV-containing NDs (i.e., with detectable PL signal) that also had detectable CL (at least 5σ above background noise) as a function of ND size. b) ND size-dependence of CL signal per NV center, normalized by calculated η to account for size-dependence of energy deposited by the electron beam. The data show no evidence of decreasing CL emission per NV due to surface effects at the smallest measured ND sizes, $d \leq 80$ nm. For large NDs in the size range $d \geq 100$ nm, the CL rate per NV varies approximately as d^{-3}. (Solid red line shows a fit of the form $S_{CL}/N_{NV}/\eta = c_1 (V_{ND}^{1/3})^{-3}$, with c_1 = (7.1 ± 0.4 S.D.) × 10^6 kcps nm^3.) We attribute this to finite carrier diffusion lengths due to high N impurity concentrations, which prevent electron–hole pairs from recombining at NV centers distant from the electron beam.

at a CL intensity corresponding to ≈20 NV centers. CL emission by the Si wafer set the background level, approximately an order of magnitude larger than the detector dark count rate. Because tissue embedded in resin for EM imaging (and likely most other biological or material samples of interest) produce CL emission rates comparable to or greater than the Si wafer,[1] our results suggest that a relatively high density of NV centers is required for ND-based correlative imaging with sub-50 nm spatial resolution under the present imaging conditions.

Finally, to investigate the average energy conversion efficiency $\bar{\xi}$ and test for intrinsic ND size-dependence beyond the number of NV centers per particle, we calculated the energy deposition efficiency η for each ND in our sample. Particle dimensions from the AFM images were used as inputs to CASINO to numerically calculate η for each ND. Dividing S_{CL} for each particle by N and the calculated η yields a corrected CL signal, proportional to $\bar{\xi}$, which we show as a function of particle size (Figure 4b). We included only NDs with CL brightness distinguishable from background for this analysis. For this subpopulation (n = 195) of NDs, we found no evidence of decreasing average energy conversion efficiency $\bar{\xi}$ at the smallest d for which we could detect CL. Thus, CL quenching and surface carrier recombination are not likely to be limiting factors for correlative CL imaging using currently available NDs.

Contrary to expectation, however, we observed a rapid decrease in energy conversion efficiency $\bar{\xi}$ (going approximately as d^{-3}) for NDs larger than ≈100 nm. We attributed the decrease in $\bar{\xi}$ for the largest NDs to short carrier diffusion lengths, known to be associated with high N impurity concentration,[23] which effectively limited the instantaneous volume over which NV centers could be excited by the SEM beam at any given scan position. To test this hypothesis, we made electron paramagnetic resonance (EPR) measurements (Figure S5, Supporting Information) on macroscopic ensembles of the NDs used in this work. These measurements indicated a N concentration on the order of 200 ppm, which should limit the carrier diffusion length to much less than $L_D < 500$ nm.[23]

7. Size Dependence of Nanodiamond CL Spectra

For applications in multicolor correlative microscopy, spectral distinguishability is another important factor in the selection of suitable nanoparticle labels. We therefore collected CL spectra from individual, NV-containing NDs of varying sizes (**Figure 5**a). The NDs selected for CL spectroscopy were obtained from the same source as the primary (n = 257) ND sample used in this work. Due to finite photon collection efficiency and limited averaging time resulting from accumulated surface contamination, we only obtained spectra for NDs of size $w > 100$ nm. ND size was parameterized for the CL spectral study by the largest transverse dimension, w, since the substrates used for these measurements prevented acquisition of correlated AFM data. We observed that for decreasing ND size, the

 © 2017 Wiley-VCH Verlag GmbH & Co. KGaA, Weinheim

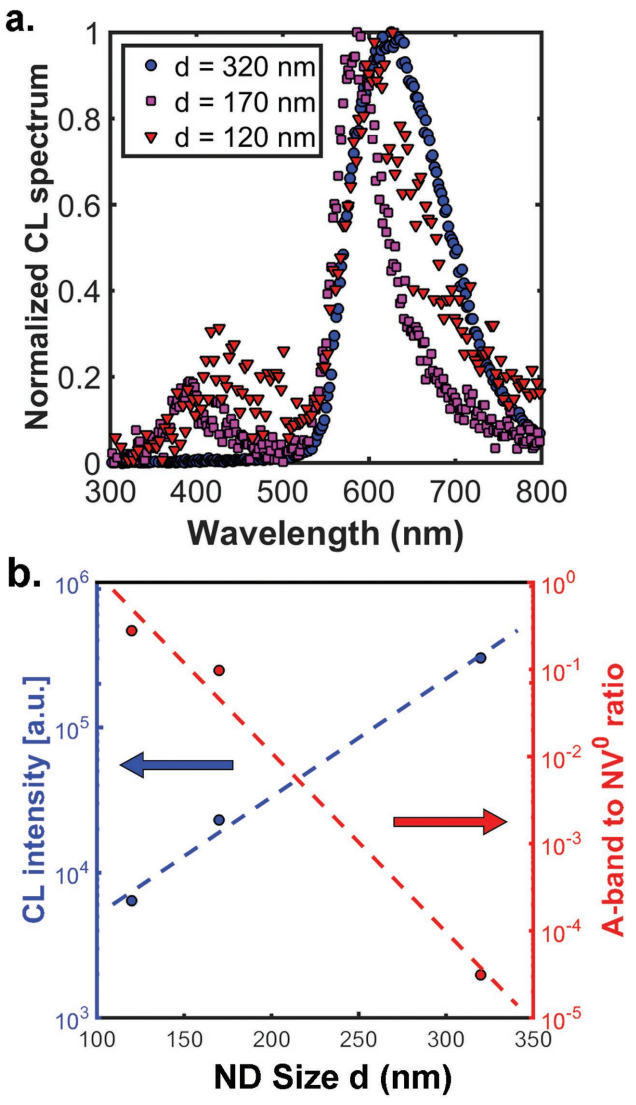


Figure 5. Effect of ND size on CL emission spectrum. a) Characteristic CL spectra for three individual NDs of various sizes, all obtained from the same source as our primary ND sample. Data are normalized to the peak value in each spectrum. Smaller NDs exhibit increased relative emission rates around wavelength $\lambda = 400$ nm. b) Effect of ND size on spectral distinguishability of NDs. Blue points represent total CL signal integrated over the full visible wavelength spectrum. Red points are the ratio of CL signal from A-band (integrated from 300 to 470 nm) to CL signal from NV centers (integrated from 550 to 750 nm).

reduction in red CL emission due to decreased NV number was accompanied by a higher fraction of CL emitted in the blue, likely associated with so-called A-band defects.[34–36] Interestingly, the absolute intensity of blue CL emission also increased in the smaller particles, from which we infer a much higher density of the physical defects such as dislocations and twinning that are associated with A-band CL in these smaller particles (Figure 5b). (Here we integrated the red CL signal over wavelengths from 550 to 750 nm, to include emission by NV^-, NV^0, as well as their phonon sidebands. The blue CL signal was integrated from 300 to 470 nm, and appears to be dominated by A-band emission.) These observations do not pose a fundamental problem for multicolor correlative imaging, since blue CL-emitting nanoparticle labels have been demonstrated with nearly zero emission in the red, thus allowing a very low threshold in the red channel to be used to distinguish between the two species.[6] Nevertheless, it may be important to consider the spectral purity of CL emission by NV-containing NDs when attempting to construct new sets of orthogonal labels.

8. Conclusion

A thorough study of the CL emission properties of NDs containing a high concentration of NV color centers for use in correlative microscopy was conducted. Because minimizing the size of the ND labels is crucial for practical applications, we attempted to isolate the mechanisms by which particle size affects CL brightness. We first carried out correlated AFM and CL imaging on a small sample of NDs, varying the electron acceleration voltage and particle size, and compared these measurements with numerical calculations made using the CASINO software to calibrate the fraction of energy deposited by incident electrons. We then performed correlated AFM, PL, and CL imaging on a larger sample which, in conjunction with the calibrated CASINO calculations, allowed us to extract the number of NV centers per ND and the efficiency of conversion from deposited electron energy to CL emission for each ND. We found that this conversion efficiency increases rapidly with decreasing particle size down to ≈80 nm, likely because the short carrier diffusion length in type Ib diamond prevents excitation of all NVs in the larger NDs. We detected CL from NDs as small as ≈40 nm, although only the brightest particles in this size range could be seen reliably above the CL background of our substrate. No systematic decrease in conversion efficiency was observed for the smallest detectable particles. (Note that our data do not rule out surface-limited conversion efficiency for even smaller particles; rather, we conclude that the current practical limit on CL detection from small NDs is set by finite NV density and CL background.) Finally, we found that the ratio of A-band (blue emission) to NV (red emission) CL increases dramatically for particles smaller than 100 nm, although this is not an important practical limitation for correlative microscopy with appropriate detection filters and image thresholding.

Given the average NV density observed in this sample, we expect that increased averaging time will allow reliable detection of a high fraction of particles in the ≈30–40 nm range. Operation at lower accelerating voltages V could also be a viable strategy to improve the relative energy deposition efficiency η for small particles while reducing background rates, although care must be taken to avoid resolution degradation due to sample charging in this case. With improvements in ND fabrication, CL imaging of even smaller labels will likely become possible. Furthermore, while the present work has focused on NV centers as a model system with well-quantified bulk PL and CL properties, we have previously identified brighter nanoparticle CL emitters (e.g., NDs optimized for A-band emission or Ce:LuAG nanophosphors),[6] which provide a promising alternative route to very high resolution CL labeling. Taken together, the results

 © 2017 Wiley-VCH Verlag GmbH & Co. KGaA, Weinheim

described here demonstrate that NDs containing NVs and other color centers are a promising marker for use in correlative microscopy.

9. Experimental Section

Nanodiamond Sample Preparation: NDs comprising the primary sample (n = 257 particles) were obtained from Academia Sinica, Taiwan.[37] The sample consisted of type 1b NDs with mean diameter ≈100 nm, and nitrogen concentration >100 ppm. The suppliers implanted these NDs with 40 keV He^+ ions at a dose of $\approx 1 \times 10^{13}$ ions cm^{-2}, then annealed at 450 C for 4 h to promote vacancy formation.[37] We suspended the NDs in deionized water, diluted to 0.01–0.001 mg mL^{-1}, ultrasonicated, and then drop-cast onto silicon wafer substrates. The substrates were first prepared by inscribing a series of 10 µm grids for coarse image registration, using photolithography (Karl Suss MJB4 Mask Aligner) and reactive ion etching (South Bay RIE-2000).

Optical Imaging: A home-built confocal microscope was used for PL characterization. ND fluorescence was excited using an Nd:YAG laser at 532 nm (intensity ≈100 kW cm^{-2}) and detected with an avalanche photodiode (APD, Perkin Elmer SPCM-AQRH-14). Two cascaded 532 nm long pass filters (Semrock) before the APD blocked excitation light while admitting NV emission (for both neutral and negative charge state). The same excitation intensity and detection path were used for all PL measurements, including (i) the calibration of single-NV fluorescence count rates, and (ii) all subsequent measurements of NV number per ND. For measurements of photon statistics to identify single NV emitters, the single APD at the end of the detection path was replaced with a unit containing a 50–50 beamsplitter and two identical APDs, one in each output arm of the beamsplitter. Relative photon arrival times between the two channels were recorded using a time correlated single photon counting module (Picoquant Picoharp 300). Autocorrelation time traces were fit according to the function $g^{(2)}(t) = 1 - (1+a)e^{-|t|/\tau_1} + ae^{-|t|/\tau_2}$.

Secondary Electron Imaging and CL Imaging: CL properties were investigated using a field emission SEM (JEOL JSM-7001F) outfitted with a spectrally-selective CL detection system.[6] Secondary electron images were used to determine particle lateral dimensions. An accelerating voltage of 5 keV was used in most experiments, unless otherwise specified. The resolved CL spectra shown in Figure 5a were obtained by feeding CL emission via multimode optical fiber to a grating spectrometer (Princeton Instruments SP2358), with another multimode fiber after the output slit feeding the light to a Perkin-Elmer APD for detection. For CL spectroscopy measurements, the sample NDs were placed on transmission electron microscope (TEM) grid substrates (Ted Pella) instead of silicon wafers, to minimize background CL emission.

Atomic Force Microscopy: An Asylum MFP-3D was used to measure the height of each ND in the direction normal to the substrate surface. An Olympus AC240TS AFM probe provided relatively high hardness and low lever spring constant, such that wear could be minimized during measurements.

Image Colocalization: By using the fabricated silicon wafers with series of 10 µm grids, the same position for PL, CL, SEI, and AFM imaging modalities (as shown in Figure S2, Supporting Information) was able to be located. Data were collected from correlated images of a total of 20 independent 10 µm × 10 µm fields of view. Custom Matlab software was used to carry out image colocalization, and 2D Gaussian fitting was performed to extract particle dimensions, as well as peak PL and CL signal intensities.

CASINO Simulation: The CASINO (monte CArlo SImulation of electroN trajectory in sOlids) software package[25,26] was used for modeling electron–sample interactions in the scanning electron microscope. Complete electron trajectories were simulated in the sample, allowing modeling of secondary electrons, backscattered electrons, absorbed energy, CL emission, X-ray emissions, and other relevant phenomena. In this work, absorbed/deposited energy information was extracted from the simulation. Each calculation was carried out with 5×10^4 simulated incident electron events, using a 5 nm diameter electron beam centered on an ellipsoidal model ND. The simulated accelerating voltage was 5 kV, unless otherwise specified.

Nitrogen Concentration Measurements: To determine ND nitrogen impurity concentrations, EPR measurements (Bruker ElexSys E500 EPR) on a 50 µL sample of NDs, with concentration 1 mg mL^{-1} were performed. NDs were dispersed in water and then transferred into a quartz EPR sample tube (2 mm thin wall, 100 mm long, Wilmad Glass Co INC, 704-PQ-100M). (2,2,6,6-Tetramethylpiperidin-1-yl)oxyl (20×10^{-6} M) was used as calibration standard to estimate nitrogen concentration. This measurement indicated an average N density of ≈230 ppm for the ND sample, which is consistent with values reported in the literature for NDs with moderately high paramagnetic nitrogen content.[38]

Supporting Information

Supporting Information is available from the Wiley Online Library or from the author.

Acknowledgements

H.L.Z. and D.R.G. contributed equally to this work. The authors thank X. Zhou, S. Gradecak, and N. Kasthuri for fruitful discussion and helpful technical assistance. This material is based upon work supported by, or in part by, the U. S. Army Research Laboratory and the U. S. Army Research Office under contract/grant number W911NF1510548, as well as by the DARPA QuASAR program under contract HR0011-11-C-0073.

Conflict of Interest

The authors declare no conflict of interest.

[1] P. de Boer, J. P. Hoogenboom, B. N. G. Giepmans, *Nat. Methods* **2015**, *12*, 503.
[2] B. G. Yacobi, D. B. Holt, *Cathodoluminescence Microscopy of Inorganic Solids*, Plenum Press, New York **1990**.
[3] B.-L. Wang, L.-I. Larsson, *Histochemistry* **1985**, *83*, 47.

 © 2017 Wiley-VCH Verlag GmbH & Co. KGaA, Weinheim

[4] B. N. G. Giepmans, T. J. Deerinck, B. L. Smarr, Y. Z. Jones, M. H. Ellisman, *Nat. Methods* **2005**, *2*, 743.
[5] S. F. Lim, R. Riehn, W. S. Ryu, N. Khanarian, C.-K. Tung, D. Tank, R. H. Austin, *Nano Lett.* **2006**, *6*, 169.
[6] D. R. Glenn, H. Zhang, N. Kasthuri, R. Schalek, P. K. Lo, A. S. Trifonov, H. Park, J. W. Lichtman, R. L. Walsworth, *Sci. Rep.* **2012**, *2*, 1.
[7] Y. Nawa, W. Inami, S. Lin, Y. Kawata, S. Terakawa, C.-Y. Fang, H.-C. Chang, *ChemPhysChem* **2014**, *15*, 721.
[8] C. M. Parish, P. E. Russell, in *Advances in Imaging and Electron Physics*, Vol. *147* (Ed: H. Peter), Elsevier, San Diego, USA **2007**, pp. 1–135.
[9] B. G. Yacobi, D. B. Holt, *J. Appl. Phys.* **1986**, *59*, R1.
[10] T. Coenen, B. J. M. Brenny, E. J. Vesserur, A. Polman, *MRS Bull.* **2015**, *40*, 359.
[11] A. C. Atre, B. J. M. Brenny, T. Coenen, A. Garcia-Etxarri, A. Polman, J. A. Dionne, *Nat. Nanotechnol.* **2015**, *10*, 429.
[12] C. G. Bischak, C. L. Hetherington, Z. Wang, J. T. Precht, D. M. Kaz, D. G. Schlom, N. S. Ginsberg, *Nano Lett.* **2015**, *15*, 3383.
[13] X. Zhou, M.-Y. Lu, Y.-J. Lu, E. J. Jones, S. Gwo, S. Gradecak, *ACS Nano* **2015**, *9*, 2868.
[14] F. J. G. de Abajo, *Rev. Mod. Phys.* **2010**, *82*, 209.
[15] H. Zhang, I. Aharonovich, D. R. Glenn, R. Schalek, A. P. Magyar, J. W. Lichtman, E. L. Hu, R. L. Walsworth, *Small* **2014**, *10*, 1908.
[16] M. W. Doherty, N. B. Manson, P. Delaney, F. Jelezko, J. Wrachtrup, L. C. L. Hollenberg, *Phys Rep.* **2013**, *528*, 1.
[17] L. Childress, R. Walsworth, M. Lukin, *Phys. Today* **2014**, *67*, 38.
[18] V. N. Mochalin, O. Shenderova, D. Ho, Y. Gogotsi, *Nat. Nanotechnol.* **2012**, *7*, 11.
[19] I. Aharonovich, A. D. Greentree, S. Prawer, *Nat. Photonics* **2011**, *5*, 397.
[20] E. Rittweger, K. Han, S. Irvine, C. Eggeling, S. Hell, *Nat. Photonics* **2009**, *3*, 1.
[21] T.-J. Wu, Y.-K. Tzeng, W.-W. Chang, C.-A. Cheng, Y. Kuo, C.-H. Chien, H.-C. Chang, J. Yu, *Nat. Nanotechnol.* **2013**, *8*, 682.
[22] G. Kucsko, P. C. Maurer, N. Y. Yao, M. Kubo, H. J. Noh, P. K. Lo, H. Park, M. D. Lukin, *Nature* **2013**, *500*, 54.
[23] T. Malinauskas, K. Jarasiunas, E. Ivakin, V. Ralchenko, A. Gontar, S. Ivakhnenko, *Diamond Relat. Mater.* **2008**, *17*, 1212.
[24] K. Kanaya, S. Okayama, *J. Phys. D: Appl. Phys.* **1972**, *5*, 43.
[25] H. Demers, N. Poirier-Demers, A. R. Couture, D. Joly, M. Guilmain, N. de Jonge, D. Drouin, *Scanning* **2011**, *33*, 135.
[26] D. Drouin, A. R. Couture, D. Joly, X. Tastet, V. Aimez, R. Gauvin, *Scanning* **2007**, *29*, 92.
[27] J. Pawley, *Handbook of Biological Confocal Microscopy*, Springer-Verlag, New York **2006**.
[28] H. Watanabe, T. Kitamura, S. Nakashima, S. Shikata, *J. Appl. Phys.* **2009**, *105*, 093529.
[29] A. Beveratos, R. Brouri, T. Gacoin, J.-P. Poizat, P. Grangier, *Phys. Rev. A* **2001**, *64*, 2.
[30] L. Rondin, G. Dantelle, A. Slablab, F. Grosshans, F. Treussart, P. Bergonzo, S. Perruchas, T. Gacoin, M. Chaigneau, H.-C. Chang, V. Jacques, J.-F. Roch, *Phys. Rev. B* **2010**, *82*, 115449.
[31] C. Bradac, T. Gaebel, C. I. Pakes, J. M. Say, A. V. Zvyagin, J. R. Rabeau, *Small* **2013**, *9*, 132.
[32] F. A. Inam, M. D. W. Grogan, M. Rollings, T. Gaebel, J. M. Say, C. Bradac, T. A. Birks, W. J. Wadsworth, S. Castelletto, J. R. Rabeau, M. J. Steel, *ACS Nano* **2013**, *7*, 3833.
[33] J. F. Ziegler, *Nucl. Instrum. Methods Phys. Res., Sect. B* **2004**, *219*, 1027.
[34] R. J. Graham, K. V. Ravi, *Appl. Phys. Lett.* **1992**, *60*, 1310.
[35] R. J. Graham, T. D. Moustakas, M. M. Disko, *J. Appl. Phys.* **1991**, *69*, 3212.
[36] D. Takeuchi, H. Watanabe, H. Sawada, S. Yamanaka, H. Ichinose, T. Sekiguchi, H. Okushi, *Diamond Relat. Mater.* **2001**, *10*, 526.
[37] Y.-R. Chang, H.-Y. Lee, K. Chen, C.-C. Chang, D.-S. Tsai, C.-C. Fu, T.-S. Lim, Y.-K. Tzeng, C.-Y. Fang, C.-C. Han, H.-C. Chang, W. Fan, *Nat. Nanotechnol.* **2008**, *3*, 284.
[38] A. I. Shames, V. Y. Osipov, J. P. Boudou, A. M. Panich, H. J. von Bardeleben, F. Treussart, A. Y. Vul, *J. Phys. D* **2015**, *48*, 155302.

Received: February 17, 2017
Revised: March 9, 2017
Published online:

© 2017 Wiley-VCH Verlag GmbH & Co. KGaA, Weinheim